Experimental and theoretical study of free-free electron-helium scattering in a CO2 laser field

D. Nehari, J. Holmes, Kevin M. Dunseath, Mariko Dunseath-Terao

Experimental and theoretical study of free-free electron-helium scattering in a CO_2 laser field

D Nehari[1], J Holmes[1], K M Dunseath[2] and M Terao-Dunseath[2]

[1] Department of Physics, St Francis Xavier University, Antigonish, Nova Scotia, Canada B2G 2W5

[2] Institut de Physique de Rennes, CNRS-UMR 6251, Université de Rennes 1, Campus de Beaulieu, 35042 Rennes Cedex, France

E-mail: `kevin.dunseath@univ-rennes1.fr`

Abstract. Free-free transitions during the scattering of electrons by helium in the presence of a linearly polarized CO_2 laser field are investigated both experimentally and theoretically. Signals for laser-assisted scattering at 22 eV with absorption or emission of up to two photons are measured at scattering angles between 20° and 70°, and are compared to the values obtained from an 11-state R-matrix Floquet calculation as well as using the low-frequency approximation of Kroll and Watson. The two sets of theoretical results are found to be in very good agreement for the scattering geometries considered in the experiment. The order of magnitude of the experimental results is reproduced by calculations with intensities in the region of 10^7 W cm^{-2}. Agreement is improved by averaging the theoretical results over the spatial distributions of the three beams as well as the temporal intensity profile of the laser pulse, and by allowing for some misalignment of the three beams in the experiment.

PACS numbers: 34.80.Bm, 34.80.Dp, 34.80.Kw, 34.80.Qb

Submitted to: *J. Phys. B: At. Mol. Phys.*

1. Introduction

Laser assisted electron-atom scattering has been an active area of research both experimentally and theoretically for some years. These processes are not only of fundamental importance to collision physics but are also relevant to applied fields such as laser heating of plasmas [1, 2]. The characteristic that distinguishes this class of elementary collision physics is that a third body (the laser photon) is present during the collision event, in addition to the electron and the target atom. This third body is characterized by parameters such as frequency, intensity, and polarization.

The challenging nature of experiments in this domain, requiring the precise alignment, focusing and synchronisation of three beams (atomic, electron and laser), has however limited the number of experimental studies [3]. Most work has been performed by Weingartshofer, Wallbank and co-workers at Saint-Francis Xavier University in Canada, using a CO_2 laser and a variety of noble gas targets (see [4–12] and references therein). From a theoretical point of view, non-perturbative treatments are generally required, even at quite moderate laser intensities. Theoretical work has been mostly limited to potential scattering or to low-frequency approximations (see for example [13–15] and the review [16]).

In this paper, we report the results of a joint experimental and theoretical study of laser-assisted electron-helium scattering, where the target atom remains in its initial state while the electron gains or loses kinetic energy through absorption or emission of photons. This process is referred to as a free-free transition since the electron undergoes a transition from one free state or continuum to another: it is also referred to as inverse bremsstrahlung for absorption and stimulated bremsstrahlung for emission. We consider the scattering of electrons by helium in the presence of a linearly polarized CO_2 laser field, at a collision energy of 22 eV, in two different scattering geometries. In the first, the electron is incident parallel to the laser polarization axis and is scattered through an angle between 20^o and 70^o (see figure 1). In the second geometry, the scattering angle is fixed at 70^o while the laser polarization is rotated in the scattering plane with respect to the direction of the incoming electron by an angle between 20^o and 70^o.

The experiment is a continuation of the work already performed by Wallbank and co-workers. Measured data are compared with numerical values from an extensive R-matrix Floquet calculation. The R-matrix Floquet approach [17–19] is applicable to many-electron targets and treats all electronic and radiative couplings in an *ab initio* and non-perturbative way, without the restrictions inherent in the low-frequency approximation. The method provides cross sections for laser-assisted inelastic collisions as well as free-free processes, while the low-frequency approximation is restricted to the latter. The R-matrix Floquet theory and associated computer codes used in this paper have been extensively tested, for instance in the case of laser-assisted potential scattering, where the results obtained were in almost perfect agreement with a completely independent method based on solving the Floquet-Lippmann-Schwinger equation [20, 21].

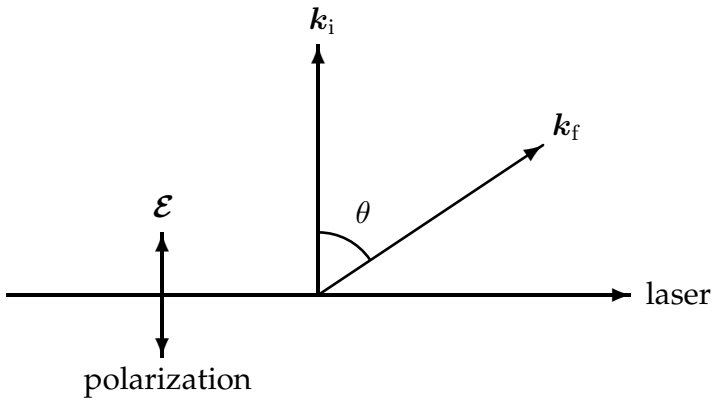

Figure 1. Experimental geometry for measurements of the free-free scattering cross section for scattering angles θ up to 70°.

The main body of the paper is organized as follows: we first present the experimental setup and the theoretical method, then compare the differential cross sections obtained using the R-matrix Floquet theory and the low-frequency approximation, in the case where the incident electron momentum is parallel to the laser polarization axis. The theoretical results are used to evaluate the free-free signal which can be compared with the experimental data. We then study the free-free process at a fixed scattering angle of 70° for different orientations of the laser polarization axis lying in the scattering plane between the incident and scattered electron momenta. In the final part, we consider the influence of the spatial distributions of the three beams as well as averaging over the temporal intensity profile of the laser pulse.

2. Description of the experiment

The experimental setup is similar to that used in earlier work by Wallbank and Holmes [5, 9, 10]. It consists of two main sections in the same differentially pumped vacuum chamber: the incident and scattered electron beams which constitute the spectrometer, and the beam of helium atoms formed by a pulsed supersonic valve behind a circular aperture 3 mm in diameter, incident at right angles to the electron scattering plane. Electrons emitted from a sharp tungsten filament are focused into a 127° cylindrical deflector which produces an electron beam with a narrow energy spread ($\approx$ 25 meV). The electrons are then accelerated and focused to produce a beam 1 mm in diameter with the required energy, 22 eV in the present experiments. The calibration of the electron beam energy was achieved using the $^2\mathrm{P}_{3/2}$ argon resonance at 11.098 eV. The electrons scattered from the atomic beam through a particular angle are then decelerated and refocused into a double hemispherical sector deflector in the 'S' configuration for energy selection, and are finally detected with an electron multiplier connected to a photon drag detector after reacceleration. In the work reported here, the overall energy resolution of the spectrometer was 55-70 meV, as measured from the full width at half maximum of

Table 1. The count rate for field-free scattering.

Scattering angle (degrees)	20	25	30	50	60	70	90	120
Count rate (x 1000 counts/second)	187	166	134	60	56	50	45	40

the peak due to elastically scattered electrons. The spectrometer is designed to detect electrons with an angular resolution of better than 2^o. The divergence of the incident beam is neglected in the estimation of the errors. Count rates for the field-free case depend on the scattering angle (see table 1): the minimum count rate that can be used to measure cross sections for free-free transitions is 20 000 counts per second. The pressure in the vacuum chamber during the measurements is about 5×10^{-6} mbar.

The radiation is supplied by a pulsed CO_2 TEA laser (wavelength 10.6 μm) operating in multi-longitudinal mode, modified by the insertion of an NaCl polarizing element in the laser cavity, which reduces the energy of the laser from 5 J/pulse to 3.4 J/pulse, together with a germanium output coupler. The pulse duration is about 3 μs and the laser focus at the scattering region has a waist of about 1 mm. The laser can run at a maximum frequency of 10 Hz, but in our experiments it is usually run at 7 Hz. The laser beam is first aligned on the scattering region using a visible low-power He-Ne laser. The position of the waist is then determined by adjusting the focusing mirror at the entrance of the vacuum chamber in order to maximize the count rate at high intensity of electrons scattered through the required angle with absorption of one photon. The interaction region is situated just after the supersonic valve. The overlap of the laser and electron beams, which are narrower than the helium beam, is carefully optimised before each measurement. The peak intensity of the laser can be up to 4×10^8 W cm^{-2} and the spatial profile is assumed to be Gaussian. A beam splitter is used in order to reflect a weak portion of the laser after the scattering region to a photon drag detector to record the profile of the laser as a function of time. Data are collected and analyzed separately during the first, second and third microseconds, thus providing information on the intensity dependence of the cross section. During the first microsecond, the average intensity is estimated to be of the order of 10^8 W cm^{-2} for about 250 ns, before falling rapidly to a few 10^7 W cm^{-2}. It remains roughly the same order of magnitude for the rest of the pulse. Further details of the setup and the experimental procedure are given in [5].

3. Description of the R-matrix Floquet calculations

Calculations of the field-free and laser-assisted differential cross sections have been performed using the R-matrix Floquet method which is described in detail elsewhere [17–19]. It provides a unified, *ab initio* and non-perturbative treatment of multiphoton ionization of complex atomic systems as well as electron-atom scattering in an intense, linearly polarized, spatially homogeneous monomode laser field. Assuming the duration of the laser pulse is much longer than that for the atomic process, the field is described

in the dipole approximation by the vector potential $\boldsymbol{A}(t) = \hat{\boldsymbol{z}}\, A_0 \cos\omega t$, where ω is the angular frequency and where we have chosen the z-axis parallel to the direction of polarization. The amplitude $\mathcal{E}_0 = A_0\omega/c$ of the electric field in atomic units is related to the laser intensity I expressed in $\mathrm{W\,cm^{-2}}$ by $\mathcal{E}_0 = \sqrt{I/I_0}$, where $I_0 = 3.51\times10^{16}\ \mathrm{W\,cm^{-2}}$. Since this time-dependent potential is periodic, the solutions of the corresponding Schrödinger equation can be expanded in terms of a Floquet-Fourier expansion:

$$\Psi(\boldsymbol{X}, t) = \mathrm{e}^{-\mathrm{i}Et} \sum_{n=-\infty}^{\infty} \mathrm{e}^{-\mathrm{i}n\omega t}\Psi_n(\boldsymbol{X}), \tag{1}$$

where $\boldsymbol{X}$ represents the set of space and spin coordinates of all the electrons, and E is the quasi-energy of the solution. Substituting this expansion into the time-dependent Schrödinger equation yields an infinite set of coupled equations for the Floquet components $\Psi_n(\boldsymbol{X})$. These are solved by adopting the standard R-matrix approach of partitioning configuration space into two regions [22]: an inner region, encompassing the charge distribution of the N-electron target states retained in the calculation, and an outer region in which the collisional electron is far from the origin so that exchange with the bound electrons can be neglected. In the inner region, the interaction of the laser field with all $N+1$ electrons is described in the length gauge, while electron exchange and correlation are included by expanding the wave function in terms of a discrete set of antisymmetrized R-matrix basis functions formed by coupling field-free N-electron target state wave functions to a set of continuum orbitals representing the remaining electron. In the outer region, the interaction of the field with the bound electrons is still described in the length gauge while the interaction with the continuum electron is described in the velocity gauge. The R-matrix on the boundary of the inner region can be expressed in terms of the eigenvalues and amplitudes of the eigenvectors of the Floquet Hamiltonian. Its inverse, the logarithmic derivative matrix, is then propagated using an adapted version of the Johnson-Manolopoulos method [23] out to some large distance, where it is used to match the wave function to the asymptotic solutions satisfying the appropriate boundary conditions. These are defined in the acceleration frame, where the the laser-electron interaction becomes vanishingly small and the equations are asymptotically uncoupled, and then transformed into the velocity gauge where they give the starting values for an asymptotic expansion. Matching to solutions satisfying scattering boundary conditions yields the reactance matrix $\boldsymbol{K}$, from which cross sections may be calculated [19].

It is important to note that the laser polarization axis breaks the spherical symmetry of the system by introducing a preferred direction in space. As a result, the total angular momentum L of the atomic system is no longer well-defined. Its projection M_L along the polarization axis is however conserved, since the system is invariant under rotation. If the incident electron momentum $\boldsymbol{k}_i$ is parallel to the z-axis, only $M_L = 0$ contributes to the cross section. In other geometries, calculations must be performed for several values of M_L. Other good quantum numbers include the total laser-atom parity Π and, since we neglect relativistic corrections, the total spin S and its projection M_S.

Table 2. Energies and energy differences for the first 11 states of helium. The accurate, non-relativistic values are taken from chapter 11 of [24]. The values of the National Institute of Standards and Technology (NIST) are taken from their Atomic Spectra Database available at http://physics.nist.gov/PhysRefData.

States	Accurate (a.u.)	Present (a.u.)	Present (a.u.)	Present (eV)	NIST (a.u.)	NIST (eV)
$1s^2$ 1^1S	−2.90372	−2.90113	0.0	0.0	0.0	0.0
1s2s 2^3S	−2.17523	−2.17493	0.72620	19.761	0.72836	19.820
1s2s 2^1S	−2.14597	−2.14405	0.75708	20.601	0.75762	20.616
1s2p 2^3P	−2.13316	−2.13243	0.76870	20.918	0.77042	20.964
1s2p 2^1P	−2.12384	−2.12220	0.77893	21.196	0.77975	21.218
1s3s 3^3S	−2.06869	−2.06859	0.83254	22.655	0.83489	22.719
1s3s 3^1S	−2.06127	−2.05881	0.84232	22.921	0.84231	22.920
1s3p 3^3P	−2.05808	−2.05788	0.84325	22.946	0.84550	23.007
1s3d 3^3D	−2.05564	−2.05560	0.84553	23.008	0.84794	23.074
1s3d 3^1D	−2.05562	−2.05558	0.84555	23.009	0.84796	23.074
1s3p 3^1P	−2.05515	−2.05409	0.84704	23.049	0.84843	23.087

The first step in an R-matrix Floquet calculation for laser-assisted scattering is therefore to define a set of field-free target states. In the work reported here, we include wave functions for the eleven lowest states of helium, given in table 2. These were obtained using the atomic structure code `CIV3` [25], which represents the wave functions by configuration interaction expansions built from a basis of atomic orbitals whose radial parts are combinations of Slater orbitals. For the states given in table 2, the orbitals have been optimized in order to calculate total cross sections for simultaneous electron-photon excitation of helium [26] and particular attention has been given to the energy differences between the excited states rather than just the absolute values of the energies. Compared to the accurate value of Pekeris [27], our ground state energy is thus slightly too high, so that the excitation thresholds in our calculation are shifted down by at most 0.07 eV compared to the values recommended by NIST. These small differences should not be important however for the case of free-free scattering at 22 eV considered here, since the collision energy is not too close to any excitation threshold and the cross section is relatively smooth. Another measure of the reliability of our wave functions is given by performing an R-matrix calculation for field-free elastic scattering. We used an R-matrix inner region of radius $40\,a_0$ and included total angular momenta up to $L = 10$, with 20 continuum orbitals per angular momentum. In figure 2, we compare the calculated differential cross sections at 20 eV and 25 eV with those measured by experiment [28, 29]. The agreement is very good for scattering angles larger than about 40°, but the differences increase to about 20% for smaller scattering angles, indicating that our wave functions do not fully account for the polarizability of the ground state. With this caveat, our target wave functions should nevertheless be adequate for the purposes of our current study, in particular for scattering angles larger than 30°.

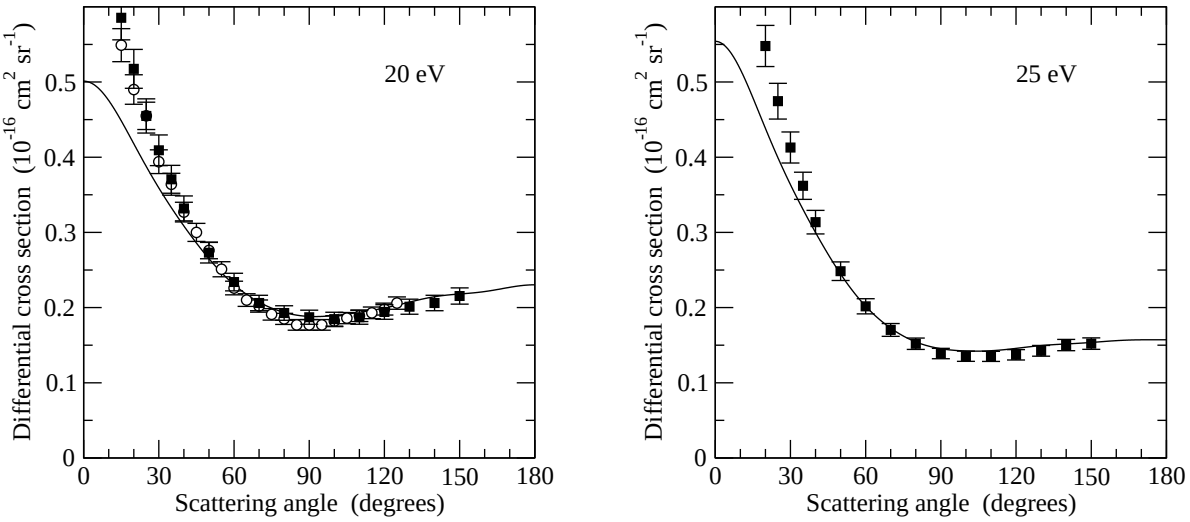

Figure 2. Comparison of experimental field-free differential cross sections with those computed by the R-matrix method including the 11 lowest states of helium. Solid line, current R-matrix calculation. Experiments: open circles, Brunger *et al* [28]; filled squares, Register *et al* [29].

4. Results and discussion

In the R-matrix Floquet calculations reported here, we retained 13 (6 emission and 6 absorption) components in the Floquet expansion (1). Total angular momenta up to $L = 15$ were included in the discrete R-matrix basis expansion. For scattering geometries in which the electron is not incident parallel to the laser polarization axis, we included all contributions with $|M_L| \leq 4$. For the largest case, $M_L = 0$, the calculations involve 351 field-dressed target states coupled with the collisional electron to give 2680 field-dressed channels. The logarithmic derivative matrix was propagated out to $250\,\mathrm{a_0}$ before matching with the asymptotic expansion. The other parameters are the same as in the field-free calculations. Convergence with respect to all these parameters has been tested, especially for the largest value of the laser field intensity (10^8 W cm^{-2}).

It should be noted that at a collision energy of 22 eV, it is possible to excite the target into the 1s2ℓ states. Our calculations show however that the cross sections for these processes are an order of magnitude or more smaller than those for free-free transitions. This is confirmed by the current experimental work: the signal for excitation was found to be several times smaller than that for free-free scattering.

4.1. Comparison between R-matrix Floquet and low-frequency approximation results

In the low-frequency approximation of Kroll and Watson [13], the differential cross section for exchange of N_γ photons is related to the field-free differential cross section

$\mathrm{d}\sigma^{\mathrm{ff}}/\mathrm{d}\Omega$ by

$$\frac{\mathrm{d}\sigma}{\mathrm{d}\Omega}^{(N_\gamma)} = \frac{k_f}{k_i} J^2_{N_\gamma}(\boldsymbol{\Delta k}\cdot\boldsymbol{\alpha}_0)\frac{\mathrm{d}\sigma^{\mathrm{ff}}}{\mathrm{d}\Omega}\,(\boldsymbol{K}_i,\boldsymbol{K}_f)\,, \tag{2}$$

where $\boldsymbol{\Delta k} = \boldsymbol{k}_f - \boldsymbol{k}_i$, $k_f^2 = k_i^2 + 2N_\gamma\omega$ and $\boldsymbol{\alpha}_0 = \alpha_0\hat{\boldsymbol{z}}$ with $\alpha_0 = \mathcal{E}_0/\omega^2$. The field-free differential cross section is evaluated for the shifted momenta $\boldsymbol{K}_{i,f} = \boldsymbol{k}_{i,f} - \boldsymbol{\kappa}$, with $\boldsymbol{\kappa} = N_\gamma\omega\boldsymbol{\alpha}_0/(\boldsymbol{\alpha}_0\cdot\boldsymbol{\Delta k})$. The main assumption made in [13] to derive (2) is that the collision occurs over a very short time compared to the period of the laser field. The approximation is valid provided that the collision geometry is such that $\mid N_\gamma/\hat{\boldsymbol{z}}\cdot\boldsymbol{\Delta k}\mid < 1$, *i.e.* away from the so-called critical geometry where the momentum transfer vector $\boldsymbol{\Delta k}$ is perpendicular to the laser polarization axis. Other approaches [15, 30] have derived the same formula by assuming that the collision energy is much larger than the photon energy. The derivation of approximation (2) also assumes that the scattering amplitude varies slowly as a function of energy. The low-frequency approximation is expected to be valid for a CO_2 laser, whose photon energy is 0.0043 a.u. (0.117 eV), and for the collision energy of 22 eV considered here.

We first consider the simple case where the incident electron is incoming parallel to the laser polarization axis. In figure 3, we compare the results of our R-matrix Floquet calculations with those of the low-frequency approximation (2), computed using the shifted momenta $\boldsymbol{K}_{i,f}$ and also by neglecting the momentum shifts $\boldsymbol{\kappa}$. Although the momentum shifts become quite large as the scattering angle decreases, the differences between the two sets of low-frequency results are very small, in particular for the range of scattering angles above 20° that interest us here. Important differences with the R-matrix Floquet results are visible below 20°, due to the fact that the latter predicts minima in the free-free cross sections at slightly larger scattering angles than in the low-frequency approximation. This shift was observed in previous calculations at lower collision energies [20, 31] but the difference seems to be larger for the higher collision energy considered here. The largest differences occur for a laser intensity of 10^8 W cm^{-2} and the net exchange of two photons, where the differential cross sections become larger than for $N_\gamma = \pm 1$. At both intensities, for scattering angles above 30°, the agreement between the R-matrix Floquet and low-frequency results is very good.

The differences visible on the logarithmic scale of figure 3 are too small to affect the comparison with the experimental data on a linear scale. This can be seen in figure 4, where we compare the free-free signal as a function of scattering angle calculated using the R-matrix Floquet theory and the low-frequency approximation (2) including momentum shifts for laser intensities of 10^7 and 10^8 W cm^{-2}. The signal is defined as the ratio of the free-free differential cross section to the field-free differential cross section, or in the case of $N_\gamma = 0$, as the ratio of their difference to the field-free cross section, expressed as a percentage of the latter. The results for net emission of one and two photons are indistinguishable from those for absorption on the scale of these figures, and are not actually plotted. The low-frequency approximation neglecting the momentum shifts predicts that these ratios are simply given by $(k_f/k_i)J^2_{N_\gamma}(\boldsymbol{\Delta k}\cdot\boldsymbol{\alpha}_0) - \delta_{0N_\gamma}$, while the comparison in figure 3 shows that this will also be a good approximation when the

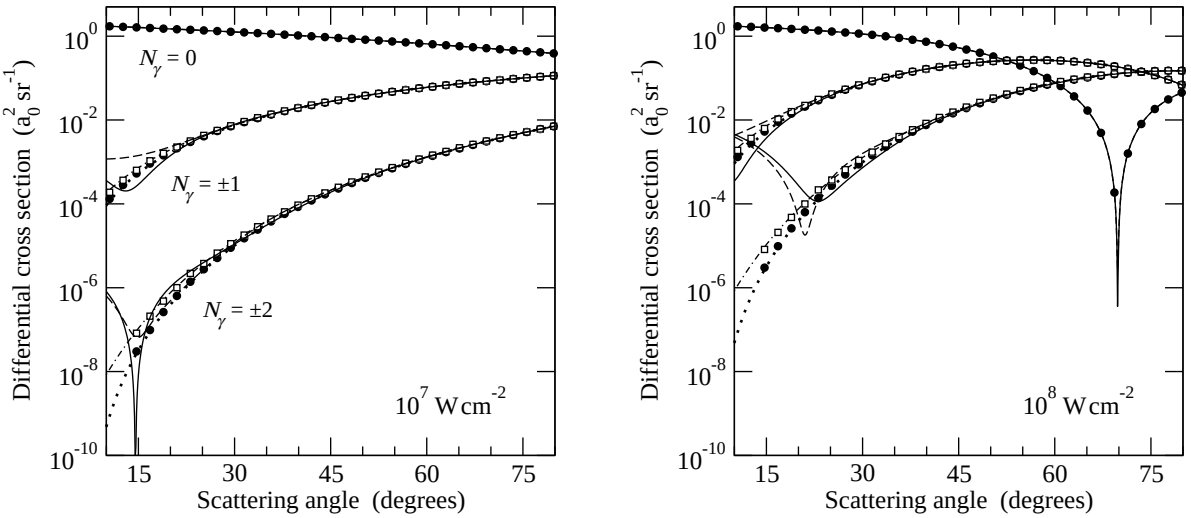

Figure 3. Comparison of differential cross sections for free-free scattering obtained using the R-matrix Floquet theory and the low-frequency approximation at intensities of 10^7 and 10^8 W cm^{-2}. Solid and dashed lines, R-matrix Floquet results for net absorption and emission of N_γ photons respectively; dotted and chain lines, low-frequency results neglecting momentum shifts; filled circles and open squares, low-frequency results including momentum shifts.

shifts are included, even relatively close to the critical geometry. The overall form of the signal, the order of magnitude of the various peaks and the positions of the mimina, simply correspond to the maxima and minima of the relevant Bessel function. Some very small differences with the R-matrix Floquet results are visible at small scattering angles, and also for angles close to 180°, but otherwise the agreement is excellent.

We remark that over the range of scattering angles considered in the experiment, the one photon absorption signal is larger at 10^8 W cm^{-2} than at 10^7 W cm^{-2}. This justifies the experimental procedure for adjusting the waist of the laser beam by maximizing the count rate of electrons scattered at high intensity.

4.2. Comparison of theoretical and experimental results for an electron incident parallel to the laser polarization axis

The experimental free-free signals at 22 eV and for scattering angles between 20° and 70° are presented in table 3. The scattering angle cannot be increased further in this configuration as the electron analyzer starts to intersect the laser beam. For net absorption ($N_\gamma > 0$) or net emission ($N_\gamma < 0$), the values given correspond to the ratios of the signals detected when the laser is on to the field-free signal, expressed as a percentage of the latter. For the case of no net exchange of photons ($N_\gamma = 0$), it is the difference of the signal with the laser on and the laser off that is expressed as a percentage of the field-free signal.

A comparison between the measured signals in each of the first three microseconds of the laser pulse and R-matrix Floquet results at different laser intensities is given in figure

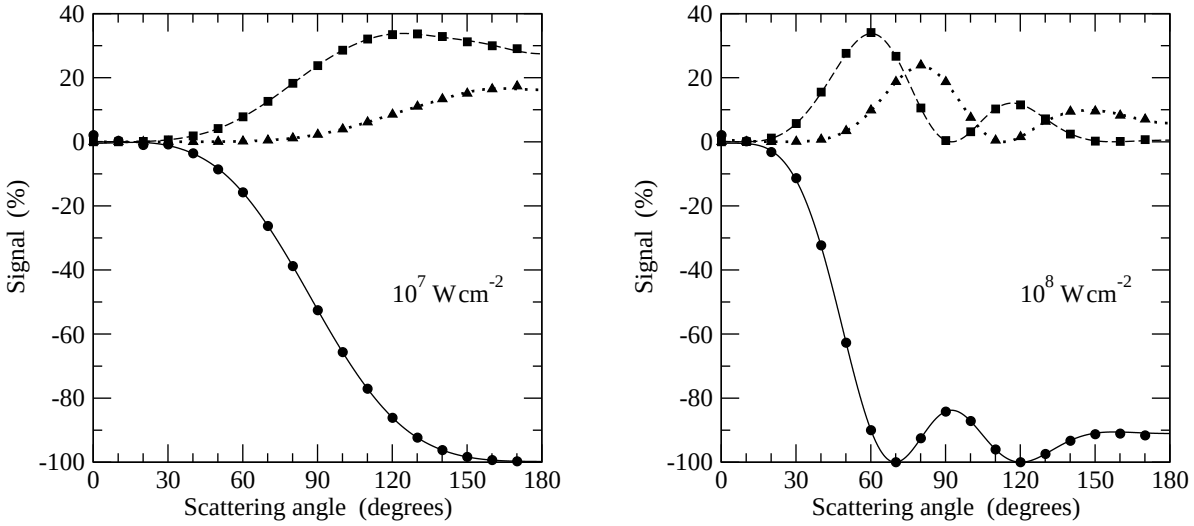

Figure 4. Comparison of free-free scattering signal computed using the R-matrix Floquet theory and the low-frequency approximation for laser intensities of 10^7 and 10^8 W cm^{-2}. R-matrix Floquet theory: ——, scattering with no net exchange of photons; - - - -, scattering with net absorption of one photon ($N_\gamma = 1$); ·····, scattering with net absorption of two photons ($N_\gamma = 2$). The corresponding results for the low-frequency approximation are given respectively by the circles, squares and triangles.

5. Clearly no one calculation at a particular intensity can reproduce all the experimental values. The overall order of magnitude of the experimental results appears to correspond to intensities much lower than 10^8 W cm^{-2}. At the larger scattering angles, the order of magnitude of the experimental results for no net exchange of photons is reproduced by the calculations for laser intensities between approximately 5×10^6 W cm^{-2} and 2×10^7 W cm^{-2}. For net absorption of one photon, the upper limit is slightly smaller, about 1.5×10^7 W cm^{-2}. It is perhaps not surprising that the experimental results for net absorption of two photons seem to correspond to slightly higher intensities: between 10^7 W cm^{-2} and about 3×10^7 W cm^{-2}. For scattering angles up to 30°, the agreement between theory and experiment appears to be better, but the signals are very small for all laser intensities.

For $N_\gamma = 0$, the experimental data at the scattering angles of 60° and 70° do not seem to follow the general theoretical trend as they present a small minimum at 60° rather than decreasing monotonically. In figure 4 however, a minimum at about 70° appears in the theoretical results at 10^8 W cm^{-2}, although its value of -100% is much lower than those measured in the experiment. For exchange of one or two photons, the experimental results tend to flatten out slightly at large scattering angles, whereas the theoretical curves in figure 4 still increase, reaching a maximum of about 34% at 60° for $N_\gamma = 1$, and 24% at about 80° for $N_\gamma = 2$. The structure in the experimental results therefore seems to suggest high laser intensities, whereas the overall orders of magnitude are more consistent with lower intensities.

Table 3. Measured values of the signal for free-free scattering at $E_i = 22\,\mathrm{eV}$, expressed as a percentage of the field-free signal. The experiment counts scattered electrons with energies $E_i + N_\gamma\omega$, so that N_γ positive refers to absorption of N_γ photons, while N_γ negative refers to emission of $\mid N_\gamma \mid$ photons. For $N_\gamma = 0$, the values given are the differences of the free-free and field-free signals, expressed as a percentage of the field-free signal. The numbers in parentheses after each value are the estimated errors.

Angle	20°	25°	30°	50°	60°	70°
			$N_\gamma = 0$			
$1^{st}\mu$s	−0.72 (0.97)	−2.15 (1.0)	−6.04 (1.08)	−13.49 (1.68)	−32.47 (1.55)	−30.47 (1.79)
$2^{nd}\mu$s	−1.9 (0.98)	−1.34 (0.99)	−3.92 (1.08)	−11.33 (1.69)	−20.49 (1.59)	−18.48 (1.82)
$3^{rd}\mu$s	−1.6 (0.97)	−1.46 (1.0)	−4.26 (1.08)	−4.0 (1.71)	−16.24 (1.62)	−13.16 (1.87)
			$N_\gamma = 1$			
$1^{st}\mu$s	0.92 (0.3)	0.92 (0.3)	2.0 (0.45)	5.58 (0.47)	10.15 (0.66)	11.88 (0.78)
$2^{nd}\mu$s	0.9 (0.3)	0.9 (0.3)	0.98 (0.44)	3.77 (0.44)	6.49 (0.59)	8.58 (0.72)
$3^{rd}\mu$s	0.79 (0.29)	0.79 (0.29)	0.25 (0.44)	3.07 (0.41)	4.97 (0.56)	5.98 (0.66)
			$N_\gamma = -1$			
$1^{st}\mu$s	0.73 (0.1)	0.96 (0.14)	1.86 (0.19)	4.75 (0.45)	11.37 (0.5)	12.56 (0.71)
$2^{nd}\mu$s	0.5 (0.09)	0.94 (0.14)	1.34 (0.16)	3.62 (0.41)	7.64 (0.43)	9.09 (0.63)
$3^{rd}\mu$s	0.54 (0.09)	0.37 (0.12)	1.16 (0.17)	2.39 (0.35)	5.67 (0.39)	6.29 (0.54)
			$N_\gamma = 2$			
$1^{st}\mu$s		0.29 (0.11)	0.39 (0.14)	0.79 (0.28)		2.65 (0.34)
$2^{rd}\mu$s		0.38 (0.11)	0.24 (0.12)	0.69 (0.19)		1.32 (0.28)
$3^{nd}\mu$s		0.3 (0.09)	0.19 (0.12)	0.33 (0.19)		0.51 (0.22)
			$N_\gamma = -2$			
$1^{st}\mu$s		0.38 (0.08)	0.52 (0.1)	1.12 (0.17)		3.42 (0.51)
$2^{nd}\mu$s		0.14 (0.07)	0.35 (0.09)	0.88 (0.21)		1.52 (0.32)
$3^{rd}\mu$s		0.16 (0.04)	0.15 (0.07)	0.36 (0.19)		0.93 (0.21)

4.3. Influence of the angle between the incident electron momentum and the laser polarization axis

In the previous sections the incident electron momentum $\boldsymbol{k}_i$ was fixed parallel to the laser polarization axis. We now fix the scattering angle at 70° and vary the angle θ_i between $\boldsymbol{k}_i$ and the laser polarization axis is such a way that the latter lies in the scattering plane between $\boldsymbol{k}_i$ and $\boldsymbol{k}_f$ (see figure 1). In the experiment, this is achieved by rotating the polarization axis. The experimental results for $N_\gamma = 0$ and $N_\gamma = \pm 1$ are given in table 4, while a comparison with the theoretical values is given in figure 6.

In the experimental configuration, the critical geometry with the momentum transfer vector almost perpendicular to the laser polarization axis occurs at about 35°. Measurements are now possible on both side of this minimum, whose position is independent of the laser intensity. On either side, the low-frequency approximation predicts that the signal varies rapidly as $(k_f/k_i)J^2_{N_\gamma}(\boldsymbol{\Delta k}\cdot\boldsymbol{\alpha}_0) - \delta_{0N_\gamma}$. The R-matrix Floquet calculations for $\theta_i \neq 0$ are much more demanding than for $\theta_i = 0$ since the differential cross section is now a coherent sum of contributions over different values of $|M_L|$ [19]. The calculations reported here include $0 \leq |M_L| \leq 4$ and have been

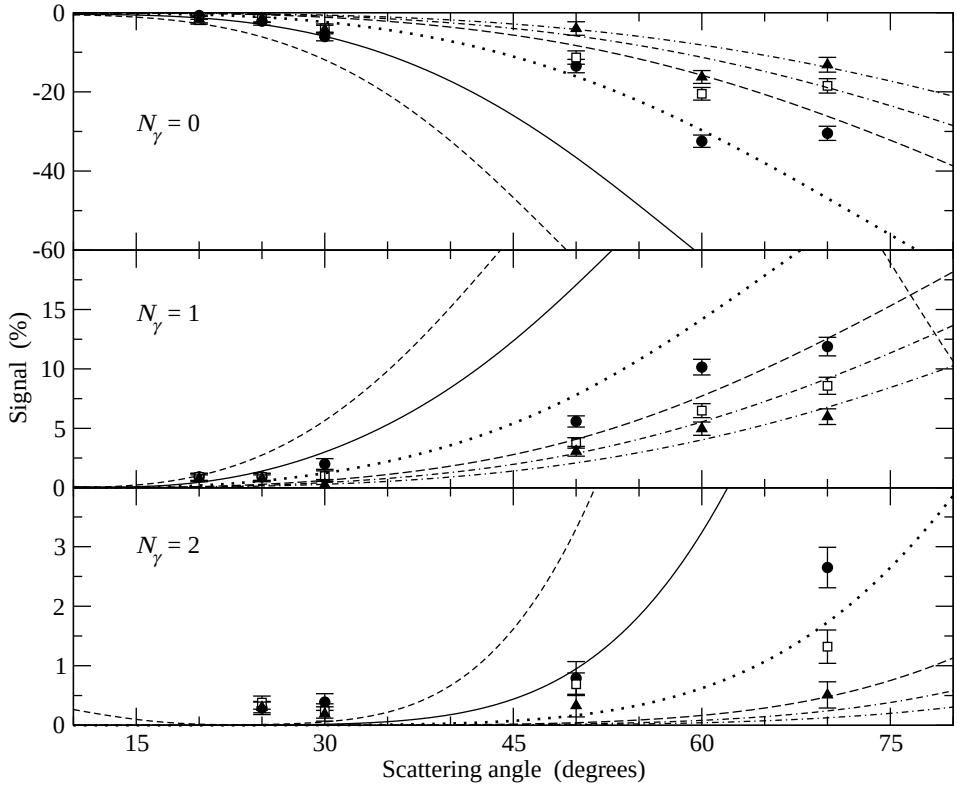

Figure 5. Comparison of experimental signals for free-free scattering with those obtained using the R-matrix Floquet theory at different laser intensities. Circles, squares and triangles are the experimental results for respectively the first, second and third microseconds of the laser pulse. R-matrix Floquet results: - - - -, 10^8 W cm^{-2}; ——, 5×10^7 W cm^{-2}; ·····, 2×10^7 W cm^{-2}; – – –, 10^7 W cm^{-2}; – – · – –, 7×10^6 W cm^{-2}; – · –, 5×10^6 W cm^{-2}.

performed for laser intensities up to $5\times10^7\,\mathrm{cm}^{-2}$. On the scale of figure 6, the signals calculated using the low-frequency approximation and the R-matrix Floquet theory are indistinguishable, as are the results for $N_\gamma = 1$ and $N_\gamma = -1$. In contrast, some of the measured values for $N_\gamma = 1$ and $N_\gamma = -1$ are noticeably different, providing a more realistic estimate of the experimental uncertainties.

The comparison with measured values again shows that calculations performed at relatively low intensities give the best agreement with the experimental orders of magnitude. The experimental results also appear to have a shallow minimum near 30°, although their values at this angle appear too large compared to theory. At $\theta_i = 70°$, the experimental signals seem to flatten out, as already observed in figure 5, especially for $N_\gamma = 0$ in the third microsecond.

Table 4. Measured values of the signal for free-free scattering at $E_i = 22\,\mathrm{eV}$, expressed as a percentage of the field-free signal, for a scattering angle of 70° and a range of angles between the incident electron momentum $\boldsymbol{k}_i$ and the laser polarization axis.

Angle	20°	30°	50°	70°
		$N_\gamma = 0$		
$1^{\mathrm{st}}\mu$s	−19.1 (2.07)	−15.62 (2.09)	−20.92 (2.27)	−36.38 (1.63)
$2^{\mathrm{nd}}\mu$s	−14.02 (2.11)	−11.81 (2.13)	−13.51 (2.29)	−23.74 (1.67)
$3^{\mathrm{rd}}\mu$s	−14.25 (2.13)	−6.49 (2.14)	−12.31 (2.33)	−11.25 (1.71)
		$N_\gamma = 1$		
$1^{\mathrm{st}}\mu$s	6.27 (0.78)	5.1 (0.76)	5.9 (1.06)	11.92 (0.7)
$2^{\mathrm{nd}}\mu$s	4.3 (0.75)	2.85 (0.73)	4.86 (1.02)	9.21 (0.66)
$3^{\mathrm{rd}}\mu$s	2.59 (0.71)	3.25 (0.74)	1.03 (0.93)	5.2 (0.63)
		$N_\gamma = -1$		
$1^{\mathrm{st}}\mu$s	6.57 (0.6)	4.22 (0.5)	5.29 (0.69)	12.54 (0.62)
$2^{\mathrm{nd}}\mu$s	4.54 (0.55)	3.76 (0.51)	2.83 (0.64)	9.46 (0.55)
$3^{\mathrm{rd}}\mu$s	4.32 (0.52)	2.69 (0.47)	3.12 (0.61)	6.43 (0.47)

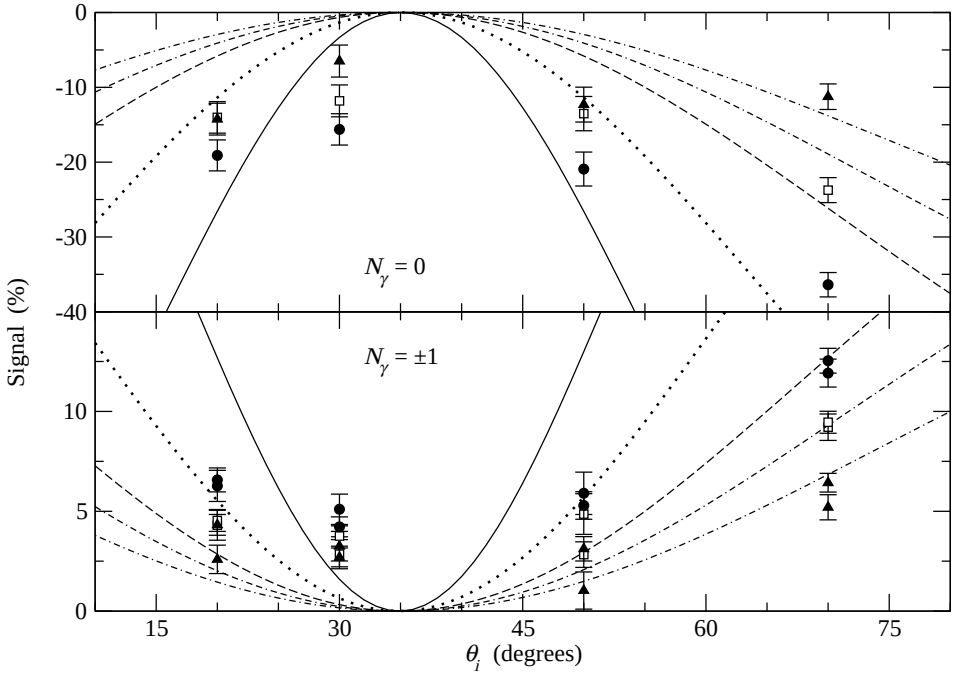

Figure 6. Comparison of theoretical and experimental signals for free-free scattering at an angle of 70° as a function of the angle θ_i between the incident electron momentum $\boldsymbol{k}_i$ and the laser polarization axis. Circles, squares and triangles are the experimental results for respectively the first, second and third microseconds of the laser pulse. R-matrix Floquet results: ——, 5×10^7 W cm^{-2}; ·····, 2×10^7 W cm^{-2}; – – –, 10^7 W cm^{-2}; – – · – –, 7×10^6 W cm^{-2}; – · –, 5×10^6 W cm^{-2}.

4.4. Averaging over the spatial distribution of the three beams and the temporal profile of the laser pulse

Previous work [32] has shown that the agreement between theory and early experiments with a strongly focused laser [33] can be improved by taking into account the spatial

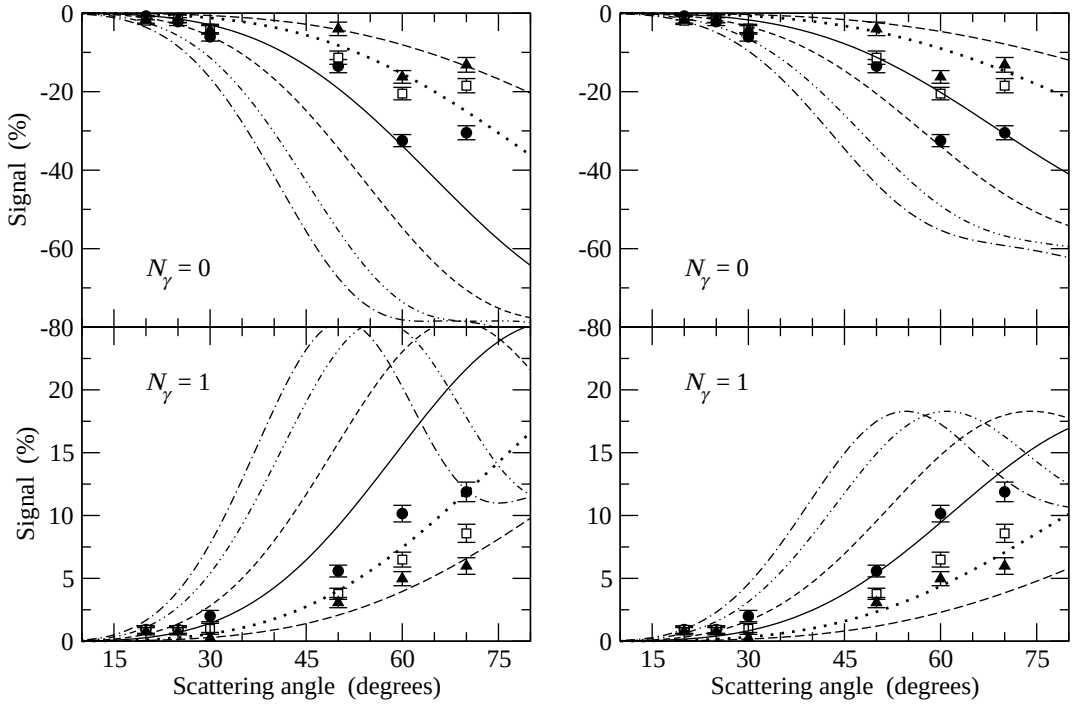

Figure 7. Signals calculated using the low-frequency approximation for various peak intensities, averaged over the interaction volume. In the left column, the three beams are perfectly aligned, while in the right column they are misaligned. The electron is incident parallel to the laser polarization axis. Circles, squares and triangles are the experimental results for respectively the first, second and third microseconds of the laser pulse. Theory: — · —, 3×10^8 W cm^{-2}; – ·· –, 2×10^8 W cm^{-2}; - - - -, 10^8 W cm^{-2}; ——, 5×10^7 W cm^{-2}; ·····, 2×10^7 W cm^{-2}; – – –, 10^7 W cm^{-2}.

and temporal distributions of the three beams involved. These effectively determine the number of scattering events occurring in regions of high or low intensities. The position of the maximum in the laser-assisted cross section depends on the laser intensity, so that different intensities will tend to favour different scattering angles.

In the low-frequency approximation, averaging over the spatial distribution of the three beams as well as over the temporal profile of the laser pulse corresponds to replacing the square of the Bessel function in equation (2) by [33, 34]

$$R_{N_\gamma} = \frac{1}{T}\int_T\int_V w(\boldsymbol{r}) J^2_{N_\gamma}(\boldsymbol{\Delta k}\cdot\boldsymbol{\alpha}_0)\,\mathrm{d}\boldsymbol{r}\mathrm{d}t$$

where T is the pulse length, V represents the interaction volume and $w(\boldsymbol{r})$ is the electron-atom density at point $\boldsymbol{r}$, normalized so that its integral over the interaction volume is equal to 1. The spatial and temporal dependencies of the intensity are contained in the quiver amplitude $\boldsymbol{\alpha}_0$.

In order to perform the spatial average for the current experiment, we suppose the laser beam to be Gaussian with a waist of 1 mm at focus. The atom and electron beams have diameters of 3 mm and 1 mm respectively, and we suppose that the particle

densities in the transverse direction also follow a Gaussian distribution. For simplicity, we only consider the scattering geometry in which the electron is incident parallel to the laser polarization axis, so that the three beams are mutually perpendicular. The divergence of the various beams and focusing effects are neglected since the relevant experimental parameters are not available. We consider two particular cases: one in which all three beams are perfectly aligned, the other in which they are misaligned by 0.5 mm, the upper limit on the alignment uncertainties in the experiment. We also allow the position of the focus to be displaced along the laser beam, so that it does not necessarily coincide with the scattering region. The results however are relatively insensitive to any reasonable values of this displacement.

In figure 7, we present the signals obtained by averaging the low-frequency approximation over the interaction volume, for net exchange of 0 or 1 photon and a range of peak laser intensities. The left column corresponds to the case in which the three beams are perfectly aligned. By comparing with figures 4 and 5, it can be seen that, as expected, spatial averaging reduces the overall order of magnitude of the theoretical results, bringing them closer to those of the experiment. At high intensities, the theoretical results for no net exchange of photons tend to flatten out in the region between 60° and 80°: the minimum appearing in the original data that corresponds to the zero of the Bessel function is effectively filled in by the spatial averaging. For the absorption of one photon, the amplitude of the peaks in the high intensity results are reduced by 60% compared to their non-averaged values. When the beams are misaligned (the right column of figure 7), the orders of magnitude are further reduced. The flattening out of the high intensity results for no net exchange of photons is less pronounced.

While the geometric properties of the three beams are relatively well-known in the present experiment, the intensity profile of the laser pulse as a function of time is more problematic. The intensity is estimated to rise to over 10^8 W cm^{-2} during the first 250 ns, before falling rapidly to a few 10^7 W cm^{-2} for the rest of the pulse. Since a detailed pulse profile on an absolute scale is difficult to establish, one can try averaging over slightly different pulse profiles in order to best fit the experimental data. The profiles tested here all have the same basic form, shown in figure 8, similar to previously published experimental profiles [7–10], but with varying values and slopes. A typical set of results for the pulse in figure 8 is shown in figure 9. In general, when the beams are perfectly aligned, the theoretical results in each microsecond are still somewhat larger than those of the experiment. For no net exchange of photons, the minimum in the results at fixed intensity due to the zero of the associated Bessel function is of course lost, and the minimum in the measured signal is not reproduced.

Much better agreement can be obtained when the beams are misaligned, particularly for the exchange of one photon at larger scattering angles during the second and third microsecond. The results for the first microsecond show the same tendency as the experiment to flatten out beyond about 70°, although they are still slightly too large. The theoretical results at lower angles tend to underestimate the experimental

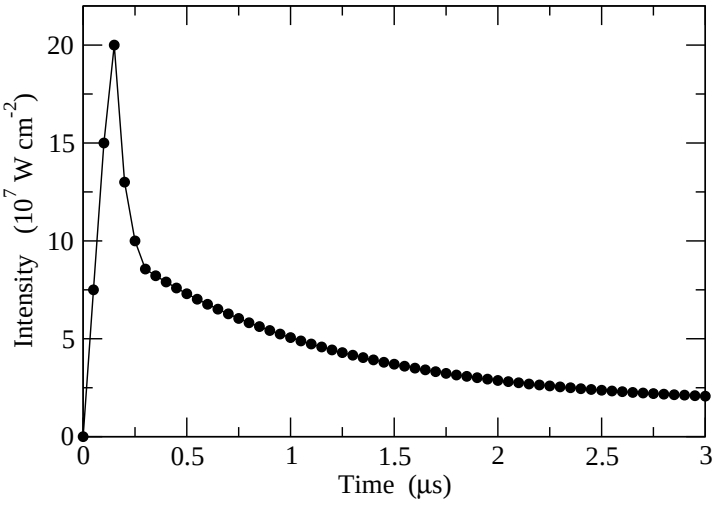

Figure 8. Laser intensity distribution used in the time-averaging of the laser-assisted signal.

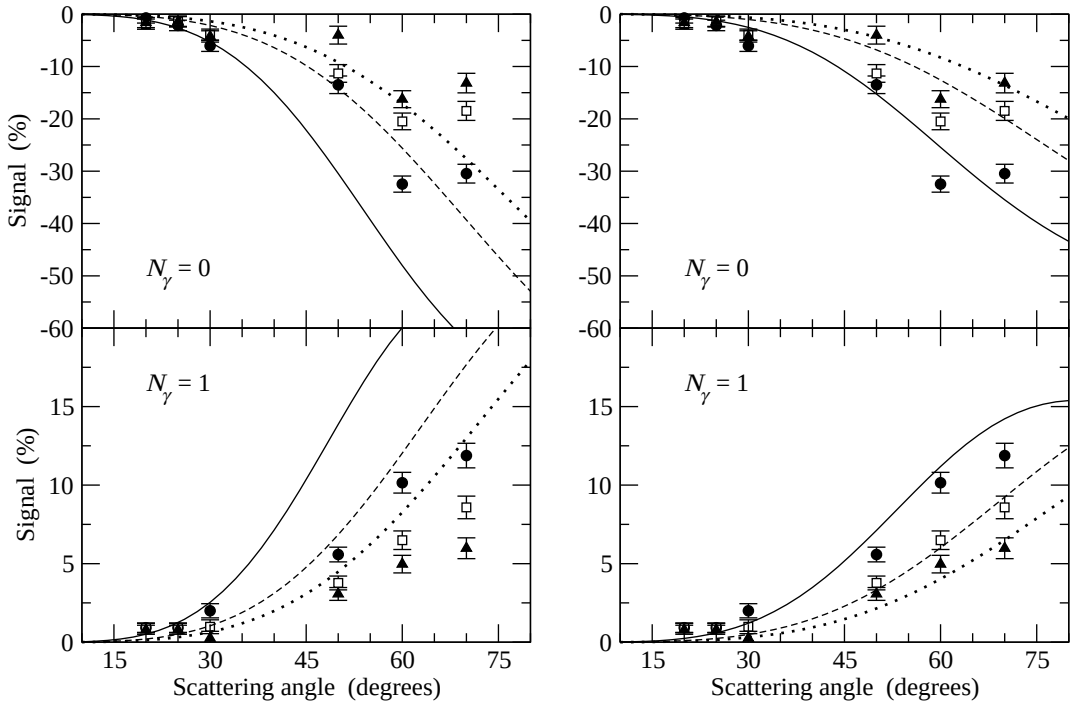

Figure 9. Signals calculated using the low-frequency approximation, averaged over the interaction volume and a model intensity distribution of the laser pulse as a function of time. The scattering geometry, experimental data and parameters in the left and right columns are the same as for figure 7. Theory: ——, first microsecond; - - - -, second microsecond; ·····, third microsecond.

results, but the actual values are very small. It should also be remembered that at these angles our field-free differential cross sections also underestimate those of experiment (see figure 2). The situation is less satisfactory for no net exchange of photons, where the minimum in the experimental data is not reproduced, although the order of magnitude is now very similar.

5. Conclusions

We have compared experimental and theoretical signals for electron-helium free-free scattering in a linearly polarized CO_2 laser field at a collision energy of 22 eV. We considered two scattering geometries, one with the incident electron parallel to the laser polarization axis for a range of scattering angles between 20° and 70°, the other with a fixed scattering angle of 70° and different angles θ_i between the incident electron momentum and the polarization axis.

The R-matrix Floquet theory and the low-frequency approximation, using the same set of eleven target states, yield differential cross sections that are in very good agreement for most of the scattering angles and laser intensities considered. When the collisional electron is incoming parallel to the laser polarization axis, the differences are seen only on a logarithmic scale near the critical geometry, in particular at higher intensities. Furthermore, there is very little difference between results calculated using the low-frequency approximation with and without momentum shifts.

At laser intensities approaching 10^8 W cm^{-2}, the calculations do not reproduce the experimental results very well, neither in order of magnitude nor the overall shape. Better agreement for the order of magnitude is obtained at lower laser intensities. The discrepancy between the measured pulse profile and the apparent average laser intensities experienced by the electrons has already been remarked upon in an earlier experiment [9] on small angle laser-assisted electron-argon scattering, and is thus confirmed by our study, albeit at larger scattering angles at a higher collision energy. In the second scattering geometry, both measured and calculated signals follow similar shapes over a wide range of incident angles θ_i, especially for absorption of one photon.

The agreement is greatly improved when the theoretical results are averaged over the spatial distribution of the three beams and the temporal intensity profile of the laser pulse. The orders of magnitude approach those of the experiment, although the detailed structure does not follow very well that of the experimental data, particularly for no net exchange of photons. The precise shape of the intensity profile as a function of time is however not well-known, so that in calculations it can be adjusted to provide the best fit to the experimental data. For scattering with net exchange of one photon, the best agreement with experiment is obtained for a peak laser intensity of 2×10^8 W cm^{-2} and when the beams are not perfectly aligned but slightly displaced.

This work has re-emphasized the need to take into account the spatial distributions of the three beams as well as their alignment and the pulse intensity profile, and hence the necessity of characterizing these properties in experimental work. From the point

of view of an inverse problem, by collecting data over a broad range of scattering angles and comparing with averaged theoretical differential cross sections, it should be possible to determine more accurately the alignment geometry in the interaction volume as well as confirming or even determining various characteristics of the laser pulse.

Acknowledgments

We would like to thank Xavier Urbain for useful discussions, and the Natural Sciences and Engineering Research Council of Canada and the St Francis Xavier University Council for Research for financial support. We would also like to acknowledge the contributions to this field made by Barry Wallbank, who unfortunately passed away just as this new experiment was starting.

References

[1] Brantov A, Rozmus W, Sydora R, Capjack C E, Bychenkov V Y and Tikhonchuk V T 2003 *Physics of Plasmas* **10** 3385–3396
[2] Wang F, Weckert E and Ziaja B 2009 *Journal of Plasma Physics* **75** 289–301
[3] Mason N J 1993 *Rep. Prog. Phys.* **56** 1275–1346
[4] Weingartshofer A, Holmes J K, Caudle G and Clarke E M 1977 *Phys. Rev. Lett.* **39** 269–270
[5] Wallbank B, Holmes J K and Weingartshofer A 1987 *J. Phys. B: At. Mol. Phys.* **20** 6121–6138
[6] — 1989 *J. Phys. B: At. Mol. Opt. Phys.* **22** L615–L619
[7] Wallbank B, Holmes J K, MacIsaac S C and Weingartshofer A 1992 *J. Phys. B: At. Mol. Opt. Phys.* **25** 1265–1277
[8] Wallbank B and Holmes J K 1993 *Phys. Rev. A* **48** R2515–2518
[9] — 1994 *J. Phys. B: At. Mol. Opt. Phys.* **27** 1221–1231
[10] — 1994 *J. Phys. B: At. Mol. Opt. Phys.* **27** 5405–5418
[11] — 1996 *J. Phys. B: At. Mol. Opt. Phys.* **29** 5881–5887
[12] — 2001 *Can. J. Phys.* **79** 1237–1246
[13] Kroll N M and Watson K M 1973 *Phys. Rev. A* **8** 804–809
[14] Krüger H and Jung C 1978 *Phys. Rev. A* **17** 1706–1712
[15] Madsen L B and Taulbjerg K 1995 *J. Phys. B: At. Mol. Opt. Phys.* **28** 5327–5342
[16] Ehlotzky F, Jaroń A and Kamiński J Z 1998 *Phys. Rep.* **297** 63–153
[17] Burke P G, Francken P and Joachain C J 1991 *J. Phys. B: At. Mol. Opt. Phys.* **24** 761–790
[18] Dörr M, Terao-Dunseath M, Purvis J, Noble C J, Burke P G and Joachain C J 1992 *J. Phys. B: At. Mol. Opt. Phys.* **25** 2809–2829
[19] Terao-Dunseath M and Dunseath K M 2002 *J. Phys. B: At. Mol. Opt. Phys.* **35** 125–140
[20] Charlo D, Terao-Dunseath M, Dunseath K M and Launay J M 1998 *J. Phys. B: At. Mol. Opt. Phys.* **31** L539–L546
[21] Kylstra N J and Joachain C J 1998 *Phys. Rev. A* **58** R26–R29
[22] Burke P G and Berrington K A 1993 Atomic and Molecular Processes: an *R*-matrix Approach (Bristol: Institute of Physics Publishing)
[23] Manolopoulos D E 1986 *J. Chem. Phys.* **85** 6425–6429
[24] Drake G W F, ed. 2006 Handbook of Atomic, Molecular and Optical Physics (New York: Springer)
[25] Hibbert A 1975 *Comput. Phys. Commun.* **9** 141–172
[26] Dunseath K M, Terao-Dunseath M and Hibbert A 2009 *J. Phys. B: At. Mol. Opt. Phys.* in preparation
[27] Pekeris C L 1958 *Phys. Rev.* **112** 1649–1658

[28] Brunger M J, Buckman S J, Allen L J, McCarthy I E and Ratnavelu K 1992 *J. Phys. B: At. Mol. Opt. Phys.* **25** 1823–1838
[29] Register D F, Trajmar S and Srivastava S K 1980 *Phys. Rev. A* **21** 1134–1151
[30] Mittleman M H 1979 *Phys. Rev. A* **19** 134–138
[31] Dunseath K M and Terao-Dunseath M 2004 *J. Phys. B: At. Mol. Opt. Phys.* **37** 1305–1320
[32] Bivona S, Burlon R, Zangaran R and Ferrante G 1985 *J. Phys. B: At. Mol. Phys.* **18** 3149–3160
[33] Weingartshofer A, Holmes J K, Sabbagh J and Chin S L 1983 *J. Phys. B: At. Mol. Phys.* **16** 1805–1817
[34] Jung C 1980 *Phys. Rev. A* **21** 408–411